Monthly Notices of the ROYAL ASTRONOMICAL SOCIETY

MNRAS **549,** 1–14 (2026)
Advance Access publication 2026 May 1

https://doi.org/10.1093/mnras/stag832

Applications of 1.4 GHz diagnostics to Type Ia Supernova host galaxies

S. Ramaiya [1]★ M. J. Jarvis [1,2] M. Vincenzi,[1] M. Sullivan [3] and I. H Whittam [1,2]

[1]*Astrophysics, Department of Physics, University of Oxford, Keble Road, Oxford OX1 3RH, UK*
[2]*Department of Physics and Astronomy, University of the Western Cape, Robert Sobukwe Road, 7535 Bellville, Cape Town, South Africa*
[3]*School of Physics and Astronomy, University of Southampton, Southampton SO17 1BJ, UK*

Accepted 2026 April 30. Received 2026 April 8; in original form 2026 March 5

ABSTRACT

Type Ia supernova (SN Ia) standardization parameters exhibit evidence for systematic variation across the host galaxy star formation rate–stellar mass (SFR$-M_\star$) plane, motivating the incorporation of galaxy SFR information in cosmological inference. SFRs are commonly estimated via spectral energy distribution (SED) fitting with far-infrared (FIR) measurements to account for dust-obscured star formation. Such FIR coverage will, however, be limited for upcoming time-domain surveys such as the Rubin Observatory Legacy Survey of Space and Time (LSST), necessitating the use of alternative SFR tracers. Here, we reconstruct the SFR–$M_\star$ plane using 1.4 GHz diagnostics, to test the consistency of host classifications against FIR-constrained SED-based estimates. Within this plane, SN Ia host galaxies are divided into three regions: Region 1 (low mass), Region 2 (high-mass star forming), and Region 3 (high-mass passive). We find that ∼84 per cent of SN hosts retain identical region assignments when using radio versus FIR-constrained SED-derived SFRs. Measuring SN Ia nuisance parameters (α, β, M) within each subregion, we find consistent values between the two SFR–$M_\star$ plane reconstructions, indicating limited sensitivity to SFR estimator choice, with the largest deviations in Region 3 at $\sim 1.1\sigma$. Across the three 1.4 GHz SFR–$M_\star$ subregions, we confirm the region-dependent variation in SN Ia standardization parameters – particularly β – reported in our earlier SED-based analysis. With near-complete radio coverage of the LSST footprint anticipated from current and forthcoming radio continuum surveys (e.g. Square Kilometre Array), radio SFR calibrations will become an increasingly useful and scalable approach to host galaxy classification, supporting the construction of robust SN Ia subsamples for precision cosmology.

Key words: supernovae: general – galaxies: evolution – infrared: galaxies – radio continuum: galaxies.

1 INTRODUCTION

Type Ia supernovae (SNe Ia) are the most direct probe of the cosmic expansion history and provide key constraints on its underlying dark energy component. In the advent of wide-field programmes such as the Vera Rubin Observatory Legacy Survey of Space and Time (LSST; Ž. Ivezić et al. 2019) and the *Nancy Grace Roman Space Telescope* (R. Hounsell et al. 2018; B. M. Rose et al. 2021), the coming decade ushers in a golden era of transient discovery, with observations of over a million SNe expected. While this discovery rate is exciting, realizing the full scientific potential of these data sets will require a coordinated effort to gather detailed environmental information for all confirmed SNe Ia. Host characterization is crucial as there is extensive evidence that SN Ia luminosities depend on their galaxy properties, with correlations observed between host stellar mass (P. L. Kelly et al. 2010; H. Lampeitl et al. 2010; M. Sullivan et al. 2010), metallicity (C. B. D'Andrea et al. 2011; M. Childress et al. 2013), and star formation rate (SFR; M. Sullivan et al. 2006, 2010) among others. A complete picture of the physical mechanisms driving these correlations, however, remains lacking, highlighting the need for continued, targeted investigation.

Informed by galaxy evolution studies, the SFR–$M_\star$ plane (e.g. E. Daddi et al. 2007; D. Elbaz et al. 2007; K. G. Noeske et al. 2007; K. E. Whitaker et al. 2012; R. Johnston et al. 2015; L. J. M. Davies et al. 2016) provides a key parameter space to study SN Ia–host correlations. The bulk of star-forming galaxies lie along a narrow sequence in this plane, known as the galaxy star-forming–main sequence (SF–MS). This relation is observed across a wide range of redshifts ($0 \lesssim z \lesssim 4$) and is typically characterized by an approximately unity slope, with an intrinsic scatter of ∼0.2−0.3 dex. Beyond this dominant self-regulated regime, the SFR–$M_\star$ plane encompasses a broader population of galaxies, ranging from elevated 'starbursts' to quiescent systems with suppressed activity. Such diversity arises from the cumulative effects of physical processes that regulate star formation, such as gas supply (G. Kauffmann et al. 2006; R. Sancisi et al. 2008), mergers (e.g. K. Bundy et al. 2009; C. J. Conselice, C. Yang & A. F. L. Bluck 2009; J. M. Lotz et al. 2011), feedback (G. Kauffmann et al. 2004; C. Dalla Vecchia & J. Schaye 2008; C. Scannapieco et al. 2008; A. C. Fabian 2012) and quenching (Y.-j. Peng et al. 2010; K. Schawinski

★ E-mail: shruti.ramaiya@physics.ox.ac.uk

et al. 2014; B. Darvish et al. 2016; L. J. M. Davies et al. 2019). A galaxy's position in this space therefore encodes information about its evolutionary state and provides a natural framework for defining physically distinct sub-populations.

Accurate measurements of the constituent observables are essential for studies of the SFR–$M_\star$ plane. While galaxy stellar masses can be estimated with relatively well-understood systematics, measuring SFRs remains considerably more challenging (see R. C. Kennicutt 1998; R. C. Kennicutt & N. J. Evans 2012 for reviews). Common star formation diagnostics, such as ultraviolet (UV) continuum and nebular emission lines (e.g. Hα), are subject to systematic limitations arising from dust attenuation and aperture-related effects (M. Sullivan et al. 2001; A. M. Hopkins et al. 2003; M. L. P. Gunawardhana et al. 2011). Infrared (IR)-based SFR tracers, by contrast, are largely insensitive to dust obscuration, as they trace dust-reprocessed stellar emission. However, in regions of largely unobscured star formation (e.g. low-dust or metal-poor systems), IR emission can provide an incomplete measure of the total SFR (e.g. D. Calzetti et al. 2007, 2010; R. C. Kennicutt et al. 2009). To mitigate the limitations from single-band diagnostics, composite SFR indicators that leverage information across multiple wavelengths – such as hybrid UV–IR measurements (e.g. K. D. Gordon et al. 2000; E. F. Bell 2003; H. Hirashita, V. Buat & A. K. Inoue 2003; J. Iglesias-Páramo et al. 2006; L. Cortese et al. 2008; C.-N. Hao et al. 2011) or full spectral energy distribution (SED) fitting (e.g. E. da Cunha, S. Charlot & D. Elbaz 2008; S. Noll et al. 2009; C. Pacifici et al. 2023) – are frequently adopted in the literature. By jointly capturing the unobscured emission from newly formed stars and the dust-reprocessed component, this approach removes the need for explicit dust-obscuration corrections.

SED fitting analyses of SN Ia host galaxies have historically relied almost exclusively on deep optical broad-band imaging from SN search and follow-up programmes. In the subset of studies that have placed SN Ia host galaxies on the SFR–$M_\star$ plane (e.g. M. Sullivan et al. 2006; H. Lampeitl et al. 2010; M. Smith et al. 2020), the SED constraints are drawn exclusively from *ugriz* photometry. In a later work, M. Sullivan et al. (2010) incorporate additional near-infrared (NIR) *JHK* photometry into their SFR–$M_\star$ plane analysis of SN Ia host galaxies where available. It is well known, however, that physical parameters inferred from SED fitting of optical/NIR photometry alone are affected by strong degeneracies (see C. Conroy 2013 for a review). The 'age–metallicity–dust' degeneracy (e.g. C. Papovich, M. Dickinson & H. C. Ferguson 2001), in particular, makes it difficult to reliably measure dust attenuation, and hence SFRs, unless far-infrared (FIR) data are available. This uncertainty can propagate into galaxy classifications, complicating the separation of passive galaxies from dust-obscured, star-forming systems. When studying SN Ia subsamples in this context, any misestimation of host galaxy properties can, in turn, lead to spurious SN Ia–host correlations or mask genuinely physical trends.

In S. Ramaiya et al. (2025, hereafter Paper I), we model the SEDs of SN Ia host galaxies in the Dark Energy Survey (DES; The Dark Energy Survey Collaboration 2005) using photometry extending to the FIR. At the time of writing, this offers the widest wavelength coverage used in studies of SN Ia hosts. We show that the mid-/FIR data are crucial for mitigating degeneracies in SED-derived SFRs and can yield significantly different estimates compared to optical-only analyses. Using these improved host galaxy property estimates, SNe Ia are classified into three distinct groups according to the distribution of their host galaxies on the SFR–$M_\star$ plane. Each region comprises galaxies at different evolutionary stages: Region 1 – low mass ($< 10^{10}$ M$_\odot$) hosts, Region 2 – high mass, star-forming hosts, and Region 3 – high mass, passive hosts. We find the colour–luminosity slope, 'β' (a SN Ia standardization parameter), is steepest for SNe Ia in Region 1 hosts ($\beta = 3.51 \pm 0.16$) and shallowest in Region 3 ($\beta = 2.12 \pm 0.16$), differing at the $\sim 6\sigma$ level. After correcting each subsample by its respective β, Region 3 SNe Ia (high mass, passive hosts) appear 0.07–0.12 mag ($> 3\sigma$) brighter, post-standardization. These findings suggest that future cosmological analyses should apply standardization relations to SNe Ia according to the region of the SFR–$M_\star$ plane their host galaxies occupy.

In this paper, we consider the feasibility of recreating the analysis in Paper I on the scale of LSST and other future time-domain surveys. In such *optical-only* survey regimes, supplementary longer-wavelength data from other facilities will be needed for measurements of SED-based SFRs. The long-wavelength data in Paper I come from the *Herschel* and *Spitzer* space telescope missions. However, within the 18 000 deg^2 LSST observing footprint, deep *Herschel* and *Spitzer* coverage is limited to a few $\sim$100 deg^2. For regions of the LSST footprint that lack mid-/FIR coverage, an alternate prescription is required to robustly measure SFRs and break degeneracies among host galaxy parameters.

One such alternative is the radio continuum, which offers a dust-unbiased tracer of star formation. Such calibrations are bootstrapped from a well-known empirical correlation between the FIR and 1.4 GHz radio emission (G. Helou, B. T. Soifer & M. Rowan-Robinson 1985; T. Jong et al. 1985; J. J. Condon 1992; M. S. Yun, N. A. Reddy & J. J. Condon 2001; E. F. Bell 2003; M. J. Jarvis et al. 2010; E. J. Murphy et al. 2011; L. J. M. Davies et al. 2017; R. H. W. Cook et al. 2024). The FIR–radio correlation (FIRC) holds over many orders of magnitude and exhibits a remarkably tight scatter ($\sim$0.3 dex), leading to the conclusion that emission at both wavelengths share a common origin (massive stars) and trace recent star formation in the local and distant universe. The FIR emission comes mostly from young, massive (> 5 M$_\odot$) type O/B stars that heat the dust in their surrounding birth clouds, which then re-radiate in the infrared. As for the radio emission at 1.4 GHz, this is mainly (non-thermal) synchrotron emission generated by cosmic ray electrons that have been accelerated by SN explosions of massive stars (> 8 M$_\odot$) (J. J. Condon 1992; E. J. Murphy 2009). The integrated radio luminosity also has a thermal component due to free–free emission from H II regions but, at 1.4 GHz, this contribution is largely negligible ($\sim$10 per cent; J. J. Condon 1992).

Radio-based star-formation calibrations will become increasingly important in the LSST era, as deep radio continuum surveys – both current and forthcoming – provide significant overlap with optical imaging. The Evolutionary Map of the Universe (EMU; R. P. Norris et al. 2011; A. Hopkins et al. 2025) will provide near-complete overlap with the LSST footprint, surveying the entire Southern hemisphere at 1.3 GHz and extending to $\delta \simeq +30^\circ$, with completion expected by 2028. In this wide-area tier, EMU together with new MeerKAT continuum programmes (e.g. S. Paul et al. 2025) will reach sufficient sensitivity to detect star-forming galaxies out to $z \sim 0.5$. In the deep drilling fields, the MeerKAT International GHz Tiered Extragalactic Exploration (MIGHTEE) survey (M. Jarvis et al. 2016; I. Heywood et al. 2022; C. L. Hale et al. 2025) has already demonstrated the power of deep radio data to probe the properties and evolution of star-forming galaxies to $z \sim 5$ (F. Tabatabaei et al. 2025; I. H. Whittam et al. 2025; N. J. Thykkathu et al. 2026; R. G. Varadaraj et al. 2026). Looking further ahead, the Square Kilometre Array Observatory (SKAO) will extend this 'wedding-cake' survey strategy to even greater depth

and angular resolution (e.g. M. Jarvis et al. 2015; I. Prandoni & N. Seymour 2015), producing radio continuum data that will detect typical SFGs to $z \sim 1$ over thousands of square degrees. Ahead of these next-generation surveys, it is vital to use existing deep radio data sets and calibrations to test the reliability of radio luminosity diagnostics as an independent SFR estimator (e.g. R. C. Arango-Toro et al. 2023) for SN Ia host galaxies.

A plan of the paper is as follows: In Section 2, we introduce the SN Ia sample and the radio data available for their host galaxies. The methodology used to derive 1.4 GHz luminosities and the selection cuts applied to obtain the final sample are also outlined. Section 3 explores the application of radio-based star-formation diagnostics in the context of SN Ia host galaxies. We present SFRs derived from SED fitting as a function of 1.4 GHz luminosity for the SN Ia host galaxies and show these data relative to radio–SFR calibrations from the literature. Adopting the calibration of R. H. W. Cook et al. (2024), we construct the SFR–$M_\star$ plane, as done in Paper I, but using 1.4 GHz SFRs in place of SED-derived estimates. This allows us to assess how consistently galaxies are assigned to the three regions identified in Paper I and to study SN Ia subsamples defined by each region. Predictions surrounding the future use of radio survey data are given in Section 4. We summarize and conclude in Section 5.

Throughout the paper, where relevant, we assume a flat Lambda cold dark matter (ΛCDM) cosmological model with $\Omega_M = 0.315$, $\Omega_\Lambda = 0.685$, and $H_0 = 70$ km s^{-1} Mpc^{-1} (following Planck Collaboration VI 2020). The radio spectral index is taken to have a value, $\alpha_{rad} = 0.7$ [1], assuming that the integrated radio emission is synchrotron-dominated at 1.4 GHz.

2 DATA AND METHODOLOGY OVERVIEW

A description of the SN Ia data sets and procedures is given in Paper I of this series. In this section, we briefly summarize the SN Ia sample for completeness and introduce the associated host galaxy radio data and analysis methods.

2.1 Supernova data

Our SN Ia data come from DES. DES is an optical imaging survey that ran for a period of 6 yr and covered ∼5100 deg^2 of the Southern hemisphere using the Dark Energy Camera (DECam; B. Flaugher et al. 2015) on the Victor M. Blanco 4-m telescope (Cerro Tololo, Chile). DES was designed to constrain the properties of dark energy using four complementary probes: galaxy clusters, weak gravitational lensing, large-scale structure and SNe Ia. For time-domain science, the DES Supernova (DES-SN) programme monitored 10 2.7-deg^2 fields in *griz* with a typical ∼7-d observer frame cadence. Eight (C1, C2, E1, E2, S1, S2, X1, X2) were 'shallow' fields, surveyed to a depth of ∼23.5 mag per epoch, and two (C3, X3) were 'deep fields', with a depth of ∼24.5 mag. This paper uses data from 'DES-SN5YR' (B. O. Sánchez et al. 2024)[2] which comprises photometrically classified SNe Ia from the full 5 yr of DES, for which spectroscopic redshifts are available for the host galaxies. Selection cuts are applied as described in Paper I to yield our primary 'gold' sample consisting of 501 SN Ia host galaxies.

[1]By convention, we define the spectral index such that the radio flux density scales with frequency as $S_\nu \propto \nu^{-\alpha_{rad}}$.
[2]https://github.com/des-science/DES-SN5YR

2.1.1 Distance estimation

SN Ia distance moduli, μ_{obs} are estimated using (e.g. R. Tripp 1998; P. Astier et al. 2006),

$$\mu_{obs} = m_x + \alpha x_1 - \beta c - M - \Delta\mu_{bias}, \quad (1)$$

where m_x, x_1, and c are the SN Ia light-curve parameters as described in the SALT3 model framework (J. Guy et al. 2007; W. D. Kenworthy et al. 2021), representing the light-curve amplitude, stretch, and colour, respectively. The light-curve fit parameters used in this analysis come from the DES-SN5YR data release[2] (B. O. Sánchez et al. 2024). The nuisance parameters α and β parametrize the stretch–luminosity and colour–luminosity relations, respectively, and M is the absolute magnitude of a SN Ia with $x_1 = 0$ and $c = 0$. Biases arising from various selection effects and choices in analysis are accounted for using the $\Delta\mu_{bias}$ term. Standard cosmological analyses include an additional term that accounts for any residual dependencies between standardized (i.e. colour- and stretch-corrected) SN Ia luminosities and their host galaxy properties. This is typically denoted by γG_{host} and defined as a step function of the form,

$$\gamma G_{host} = \begin{cases} +\gamma/2 & P > P_{step}, \\ -\gamma/2 & \text{otherwise}, \end{cases} \quad (2)$$

where γ is the residual 'step' size, P is a chosen property of the SN host galaxy and P_{step} is the threshold value defining the step. It is usual in cosmological analyses of SNe Ia to take the stellar mass as the host galaxy property, with the step measured on either side of a $10^{10}M_\odot$ threshold (i.e. the 'mass step'; P. L. Kelly et al. 2010; H. Lampeitl et al. 2010; M. Sullivan et al. 2010). In the interest of studying correlations between SNe Ia and their host galaxies, we do not use this term in our analysis. Here, SNe Ia in low- and high-mass galaxies are fit *separately* and therefore this mass step term is simply absorbed by M.

We further note that the robustness of our results against selection effects was explored in our earlier work using both the full DES-SN sample (up to $z \sim 1.2$) and a redshift-restricted sample ($z < 0.6$), where such effects are expected to be significantly reduced. This test is not repeated here and we refer the reader to Paper I (their section 2; results in their table 4).

2.2 Galaxy data

MeerKAT is a 64-dish radio interferometer located in South Africa, with each receptor comprising a 13.5-m diameter main reflector and a 3.8-m diameter sub-reflector. The telescope is equipped with receivers operating across three frequency bands: UHF-band ($580 < \nu < 1015$ MHz), L-band ($900 < \nu < 1670$ MHz), and S band ($1750 < \nu < 3500$ MHz). Our radio continuum data come from the MIGHTEE (M. Jarvis et al. 2016) survey, which is one of the Large Survey Projects currently being conducted with MeerKAT. It is mapping ∼20 deg^2 across four extragalactic legacy fields: Chandra Deep Field-South (CDFS), Cosmic Evolution Survey Deep Field (COSMOS), ELAIS–S1, and XMM-Large Scale Structure (XMM-LSS). The L-band receiver is being used for the bulk of the survey work, reaching a nominal sensitivity of $\sim 4\mu$Jy, with additional observations made over a smaller area with the S-band receiver. The survey simultaneously provides radio continuum (e.g. I. Heywood et al. 2022; I. H. Whittam et al. 2022; C. L. Hale et al. 2023, 2025), spectral line (e.g. N. Maddox et al. 2021; A. A. Ponomareva et al. 2021, 2023; I. Heywood et al. 2024), and polarization

(e.g. K. Böckmann et al. 2023; A. R. Taylor et al. 2024) data, allowing a broad range of science topics to be addressed.

2.2.1 Catalogues and photometric flux measurements

The first step in our analysis is to identify the fraction of our sample (501 DES-SN hosts) that have associated radio observations. We use host galaxy matched catalogues compiled by Hale et al. (in preparation), which provide K_s-band selected counterparts for the radio detected sources in MIGHTEE data release 1 (DR1). The radio sources were associated with the optical/NIR counterpart using a combination of likelihood-ratio technique (e.g. K. McAlpine et al. 2012) and visual inspection to cross-match extended sources. At present, the catalogues cover three of the four MIGHTEE fields: COSMOS, CDFS, and *XMM*-LSS (C. L. Hale et al. 2025), but here we only consider the latter two (see Paper I for a justification). The DES-SN host galaxy coordinates are positionally cross-matched to the Hale et al. (in preparation) catalogue sources using a 1 arcsec matching radius to the K_s-band right ascension and declination, as opposed to the radio counterpart positions, which have a slightly poorer astrometric accuracy due to the lower angular resolution. Of the total sample, 95 DES-SN hosts have corresponding radio observations in the Hale et al. (in preparation) catalogues.

The Hale et al. (in preparation) catalogues only include objects in the MIGHTEE fields that are 'detected' in the radio. The standard catalogue selection corresponds to a peak flux density threshold of 5σ (see C. L. Hale et al. 2025 for details). Only considering sources that have significant detections at this wavelength introduces a bias towards studying massive star-forming galaxies (SFGs) and/or active galactic nuclei (AGNs). To mitigate this bias and derive a more *complete* sample that includes radio 'non-detections', we additionally measure photometry for all DES-SN host galaxies that overlap with the MIGHTEE image footprint in CDFS and *XMM*.

Radio photometry is performed on MIGHTEE *L*-band images (C. L. Hale et al. 2025), which are calibrated in units of Jy beam^{-1}. MIGHTEE DR1 includes both low- [7.3 and 8.9 arcsec beam full width at half-maximum (FWHM)] and high-resolution (5.5 and 5.0 arcsec beam FWHM) images across CDFS and XMM, respectively. We perform photometry on the high-resolution images across both fields. However, in practice, source fluxes at the redshifts of the DES sample ($z < 1.2$) are expected to vary little with image resolution, since the host galaxies are unresolved at both resolutions. We confirm that this is indeed the case. To extract fluxes, we measure the pixel value at the positions of the DES-SN host galaxies, which represent the total flux density of a point source positioned at the centre of that pixel.[3] The flux values are median background-subtracted. The associated errors are derived via a two-step process. First, a background distribution is determined by measuring the values in the nearest 500 pixels (an arbitrary choice) to each source position. At these wavelengths, source confusion from multiple unresolved galaxies within a single MeerKAT beam results in a skewed normal background distribution, characterized by an excess of positive source counts. Therefore, the second step in determining the error on the MIGHTEE fluxes is to fit the distribution with an asymmetric Gaussian. We take the right-hand side i.e. larger standard deviation, as our error term (a conservative choice) to account for the issue of source confusion. This yields radio flux measurements for 372 DES-SN galaxies. For this, we use flux measurements from Hale et al. (in preparation) where possible (95 galaxies), and our forced-photometry measurements for the remaining. 129 DES-SN host galaxies fall outside the currently available data from the MIGHTEE survey and do not bias our results in any way. Any additional selection cuts applied at later stages of the analysis are discussed in the relevant sections.

[3]The assumption that underlies this is that the sources are unresolved, which holds true for the bulk of our sample.

2.2.2 1.4 GHz luminosity

Host galaxy radio flux densities are converted to rest-frame 1.4 GHz radio luminosities using,

$$L_{\nu_{\rm em}} = \left(\frac{\nu_{\rm obs'}}{\nu_{\rm em}}\right)^{\alpha_{\rm rad}} S_{\nu_{\rm obs'}} (1+z)^{\alpha_{\rm rad}-1} 4\pi D_{\rm L}^2, \quad (3)$$

where $\nu_{\rm em}$ is the frequency at which the radiation is emitted in the rest frame, $\nu_{\rm obs'}$ is the frequency at which observations are taken, $\alpha^{\rm rad}$ is the radio spectral index, $S_{\nu_{\rm obs'}}$ is the flux density, and $D_{\rm L}$ is the luminosity distance of the source. We take $\nu_{\rm em} = 1.4$ GHz which is a standard reference frequency in radio continuum astronomy due to the wide availability of *L*-band observations. Due to the wide bandwidth of the *L*-band receiver on MeerKAT and the large primary beam (field of view), the effective observed frequency varies across the field, therefore $\nu_{\rm obs'}$ is determined by measuring the pixel value at the positions of the DES-SN host galaxies on the MIGHTEE effective frequency maps (C. L. Hale et al. 2025). We fix the redshift of each galaxy to the spectroscopic host redshift from the DES-SN5YR data release[2]. The errors on radio luminosities are propagated from the measured uncertainties on the radio flux density.

2.2.3 AGN selection cuts

Radio continuum diagnostics provide a useful tracer of star formation, unbiased by the effects of dust obscuration, but they are not entirely without limitation. In addition to star formation processes, the observed radio output can be generated by AGNs. The impact this has on our ability to estimate the SFR is twofold: (i) it contributes to the scatter in the conversion from radio luminosity to SFR, and (ii) it can lead to an overestimate of the SFR due to the contribution from a central AGN.

In this work, we remove potential AGN-like sources in the following way. The radio luminosity that AGNs typically begin to dominate the source counts occurs at around $L_{1.4} > 10^{23.5}$ W Hz^{-1} (e.g. T. Mauch & E. M. Sadler 2007; R. J. Wilman et al. 2008). Of our total sample, eight objects are identified above this threshold and are represented by open circles in all figures. Further inspection of the MIGHTEE radio maps shows two more objects that lie below this threshold but display clear morphological signs of AGN activity in the radio maps i.e. jet-like phenomena. These are represented by open stars in all figures and we omit all 10 objects from subsequent analyses, yielding a final sample comprised of 362 DES-SN galaxies.

More sophisticated methods of identifying AGNs are often applied to deep radio surveys (e.g. I. H. Whittam et al. 2022), but these generally rely on having deep data at other wavelengths, beyond the optical and NIR. We therefore, do not use them here as our aim is to emulate what will be feasible with the data available

across the wide-field survey of LSST. Although we note, such data, where available, could be used to increase sample purity.

3 APPLICATIONS OF 1.4 GHz DIAGNOSTICS TO TYPE IA SUPERNOVA HOST STUDIES

3.1 Introduction

The physical interpretation of radio continuum emission as a tracer of star formation relies on calibration against independent SFR indicators. Calibrations are usually anchored to FIR emission through the tight radio–infrared correlation (referenced to 1.4 GHz for synchrotron-dominated radio emission, e.g. J. J. Condon 1992; M. S. Yun et al. 2001; E. F. Bell 2003; M. J. Jarvis et al. 2010). Independent of FIR-based approaches, recent work (e.g. L. J. M. Davies et al. 2017; D. J. B. Smith et al. 2021; R. H. W. Cook et al. 2024) has begun to shift its focus to calibrating the SFR–radio relation using SFRs inferred from full SED modelling. This approach combines FIR constraints with information at other wavelengths and is therefore expected to provide a more representative measure of the total star formation, while also allowing a more robust treatment of the associated uncertainties (L. J. M. Davies et al. 2016). An illustrative example of this methodology is presented by R. H. W. Cook et al. (2024), who derive SFRs from PROSPECT-based (A. S. G. Robotham et al. 2020) SED modelling, with recent activity characterized by the $\mathrm{SFR}_{\mathrm{burst}}$ parameter, averaged over a 100 Myr time-scale. Their analysis considers a volume-limited sample of ∼5500 SFGs, combining 1.4 GHz radio data from the MIGHTEE survey – also used in this work – with ancillary survey data. Following their detailed investigation, we adopt the prescription derived therein

$$\frac{\mathrm{SFR}}{\mathrm{M}_{\odot}\mathrm{yr}^{-1}} = 10^{1.014\pm0.003} \cdot \left(\frac{L_{1.4\ \mathrm{GHz}}}{5\times10^{22}\mathrm{WHz}^{-1}}\right)^{0.868\pm0.005} \quad (4)$$

We note that this specific calibration choice is not unique, and alternative physically motivated formulations exist (e.g. J. J. Condon 1992; E. F. Bell 2003; A. M. Hopkins et al. 2003; A. Boselli et al. 2015; L. J. M. Davies et al. 2017); however, many of these either rely on calorimetric assumptions (J. J. Condon 1992) or are traditionally anchored to SFRs inferred from single- or limited wavelength diagnostics (E. F. Bell 2003). While L. J. M. Davies et al. (2017) adopt a similar SED-based approach, their calibration is derived from a significantly smaller sample of 144 galaxies (cf. ∼5500 in R. H. W. Cook et al. 2024).

We do not re-derive an SFR–$L_{1.4}$ calibration in this work as our galaxy sample is defined according to explicit criteria (Section 2) and does not include all sources within the relevant redshift range (i.e. not volume-complete). This has the potential to introduce selection-driven biases into any inferred relation. Moreover, the future applicability of 1.4 GHz SFRs to SN Ia host galaxy studies will likely rely on existing calibrations rather than those derived from the host samples themselves. The R. H. W. Cook et al. (2024) calibration therefore provides a suitable external reference for our primary aim – assessing whether radio emission can be used to separate galaxies by their star-forming properties in the context of this science.

Although we do not attempt to derive a new calibration here, it is nevertheless informative to examine the distribution of our SN host galaxies relative to the R. H. W. Cook et al. (2024) relation for consistency. This comparison combines $L_{1.4}$ values measured in this work (Section 2) with SED-derived SFRs taken from Paper I. Briefly, these SFRs are inferred using the BAGPIPES SED fitting code (A. C. Carnall et al. 2018) together with the updated 2016 G. Bruzual & S. Charlot (2003) stellar population synthesis models and a P. Kroupa (2001) initial mass function (IMF). For the remaining user-specified parameters, we assume a log-normal star formation history and a S. Charlot & S. M. Fall (2000) dust attenuation law with a variable slope i.e. the fiducial model in Paper I and we refer the reader there for full details and priors.

Fig. 1 shows the SFR–$L_{1.4}$ relation for our SN host galaxies using SED-derived SFRs from BAGPIPES, together with residuals shown relative to the R. H. W. Cook et al. (2024) calibration (gold solid line). This relation is presented for two SED fitting configurations: the left panels use SFRs derived from fits to the full multiwavelength data set available in Paper I, including *Herschel* and *Spitzer* ('HS') measurements, while the right panel shows the same relation for SFRs derived without these FIR data ('NHS' stands for 'No *Herschel* and *Spitzer*'). This HS/NHS notation is used consistently for other SED-derived quantities throughout the paper.

For clarity, the axes are truncated and shown in logarithmic scale; sources lying outside the plotted range, as well as objects with negative 1.4 GHz flux densities, are not displayed. Error bars are also removed for clarity. As Fig. 1 is used solely to illustrate the relative distributions of galaxies in the HS versus NHS cases, these visualization choices do not affect any subsequent results or analysis, which makes use of the full galaxy sample irrespective of whether individual sources appear in this figure specifically.

Several other literature calibrations from J. J. Condon (1992), E. F. Bell (2003), and L. J. M. Davies et al. (2017) are overplotted for reference. For consistency with Paper I, all relations are scaled to a P. Kroupa (2001) IMF, using conversions outlined in P. Madau & M. Dickinson (2014), for E. E. Salpeter (1955) and G. Chabrier (2003), and D. B. Haarsma et al. (2000) for G. E. Miller & J. M. Scalo (1979).

The HS and NHS configurations are shown to illustrate the sensitivity of the inferred SFRs – and hence the appearance of the SFR–$L_{1.4}$ relation – to the available wavelength coverage used in SED fitting. In the HS configuration (left panels of Fig. 1), the SED-derived SFRs show broad agreement with the R. H. W. Cook et al. (2024) relation (equation 4) across the sampled range in $L_{1.4}$, with residuals ($\Delta\mathrm{SFR} = \mathrm{SFR}_{\mathrm{SED}} - \mathrm{SFR}_{\mathrm{Cook}}$) approximately centred on zero, having a median of 0.42 $\mathrm{M}_{\odot}\,\mathrm{yr}^{-1}$, a 16th–84th percentile range of [−1.72, 6.12] and an r.m.s scatter, $\sigma_{\Delta\mathrm{SFR}} = 8.61 \pm 0.64\ \mathrm{M}_{\odot}\,\mathrm{yr}^{-1}$. In the absence of FIR data (right panels of Fig. 1), the SFR estimates are subject to stronger degeneracies with dust attenuation and stellar population age, allowing a wider range of star formation histories to reproduce the observed optical–NIR photometry. This manifests as the inferred SFRs displaying markedly increased scatter and a systematic offset towards higher values relative to the R. H. W. Cook et al. (2024) relation (see Paper I, section 6), with a broader residual distribution, characterized by a median of 8.48 $\mathrm{M}_{\odot}\,\mathrm{yr}^{-1}$, a 16th–84th percentile range of [−0.10, 37.7] and an r.m.s scatter, $\sigma_{\Delta\mathrm{SFR}} = 44.3 \pm 3.30\ \mathrm{M}_{\odot}\,\mathrm{yr}^{-1}$. Taken together, this comparison underscores how SED-fitting choices can propagate into the radio–SFR relation, with direct implications for studies that seek to calibrate or interpret them.

3.2 1.4 GHz SFR–M_* plane

Using the SFR−$L_{1.4}$ calibration from R. H. W. Cook et al. (2024), we construct the 1.4 GHz SFR–$M_{\star}$ plane (Fig. 2) for our sample of DES-SN hosts. This figure is intended as a replica of fig. 7 in

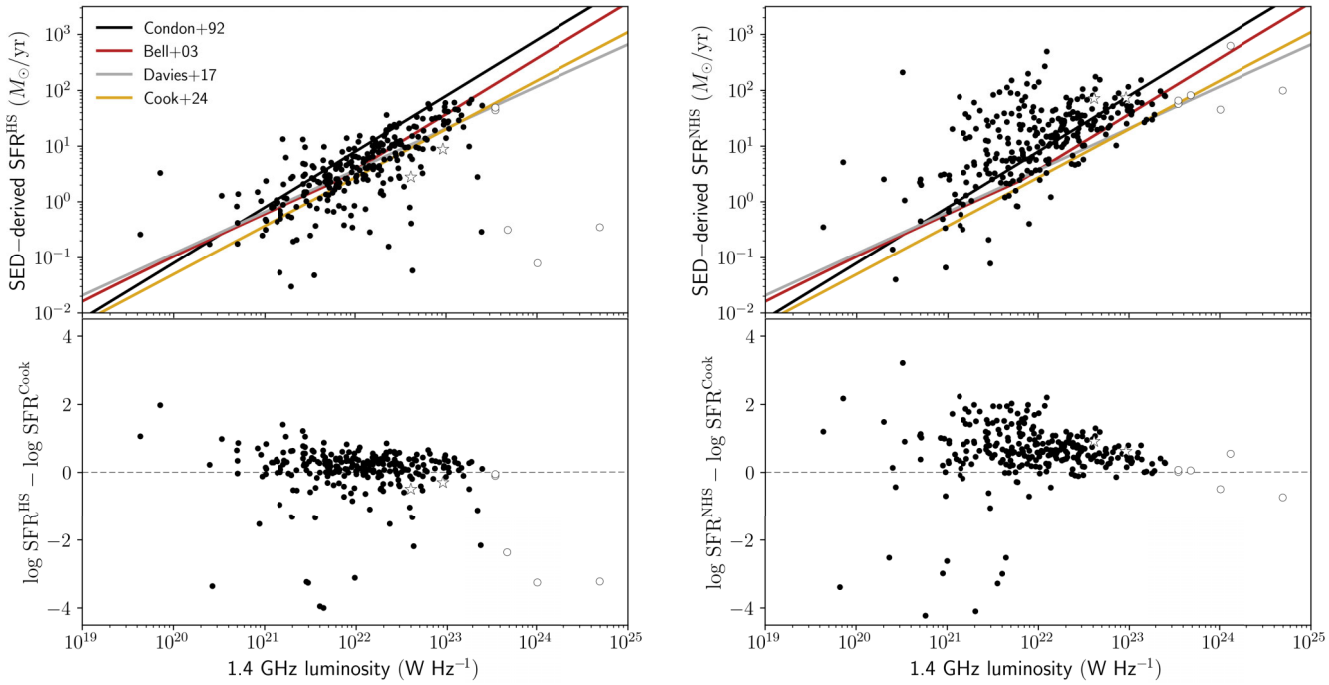

Figure 1. *Left*: SFR$^{\rm HS}$ determined from SED fitting of multiwavelength data (values taken from Paper I) versus 1.4 GHz radio luminosity, $L_{1.4\,\rm GHz}$ (computed in this work). The SED-derived estimates are from fitting data that include far-infrared coverage, specifically from the *Spitzer* and *Herschel* space telescopes (denoted by 'HS'; see Paper I). Overplotted are several reference SFR–$L_{1.4\,\rm GHz}$ calibrations from the literature (J. J. Condon 1992; E. F. Bell 2003; L. J. M. Davies et al. 2017; R. H. W. Cook et al. 2024). The open circles represent sources with $L_{1.4} > 10^{23.5}$W Hz^{-1}, i.e. in the AGN–luminosity regime, and the open stars are objects with morphological signs of AGN activity in the radio maps (Section 2). Error bars are removed for clarity. *Right*: As left, except the far-infrared data are excluded when deriving SFR from SED fitting ('NHS' refers to 'No *Herschel* and *Spitzer*').

Paper I, but with 1.4 GHz SFRs in place of BAGPIPES SED-based SFRs. The stellar masses are still computed from SED-fitting and are taken from Paper I, with one exception; *Herschel* and *Spitzer* data are excluded from their computation. This is to assess the reproducibility of the SFR–$M_\star$ relation presented in Paper I for LSST sources lacking mid-/FIR coverage.

Next, we split the 1.4 GHz SFR–$M_\star$ plane into three regions. The first region comprises SNe Ia in low-mass hosts, where we define the threshold between low- and high-mass hosts at 10^{10}M$_\odot$. To split high-mass hosts into star-forming versus passive systems, we adopt the parametric form of the SF–MS presented in K. E. Whitaker et al. (2012). While alternative parametrizations exist (e.g. J. S. Speagle et al. 2014; K. E. Whitaker et al. 2014; C. Schreiber et al. 2015), we choose the K. E. Whitaker et al. (2012) relation to maintain internal consistency with Paper I, ensuring that any regional differences can be attributed solely to the change in SFR tracer, rather than to shifts in the classification scheme. In its mathematical form, the SF–MS is expressed as,

$$\log_{10}[\mathrm{SFR}(z)] = \alpha(z)[\log_{10}(M_\star) - 10.5] + \beta(z), \quad (5)$$

where $\alpha(z)$ and $\beta(z)$[4] parametrize the slope and normalisation of the SF–MS, respectively and are given by,

$$\alpha(z) = \alpha_1 + \alpha_2 z$$
$$\beta(z) = \beta_1 + \beta_2 z + \beta_3 z^2$$

with fit parameters: α_1, α_2, β_1, β_2, and β_3. We take the median values presented in table 3 in R. Johnston et al. (2015). Adopting this parametrization, the second region isolates galaxies that lie within a 3σ interval of the SF–MS (this applies only to galaxies below the SF–MS, not above it). We take $\sigma = 0.3$ dex following R. Johnston et al. (2015) (hence $3\sigma = 0.9$ dex). The third and final region, consists of passive galaxies that have evolved off and lie $> 3\sigma$ below the SF–MS. Full details are presented in Paper I.

[4]These α and β parameters are not to be confused with those used to characterize the SN stretch– and colour–luminosity relations.

3.2.1 *Comparison to Paper I regions*

The three region subsamples (low-mass SF, high-mass SF, and high-mass passive) from this work can now be compared to those from Paper I using a confusion matrix to assess the level of consistency between the two classification schemes (Fig. 3, left panel). The Paper I region assignments, based on SED-derived SFRs and stellar masses including *Herschel* and *Spitzer* ('HS'), are treated as the reference (y-axis). Importantly, the classification shown on the y-axis should not be interpreted as an absolute ground truth, but rather as a higher-information reference against which we assess the consistency of alternative selection methods. Equivalent confusion matrices constructed using radio–SFR calibrations alternative to R. H. W. Cook et al. (2024) are presented in Appendix A.

The resulting confusion matrix is strongly dominated by the diagonal, with ∼84 per cent of DES-SN hosts retaining the same regional classification between this work and Paper I. To interpret the consistency of individual regions, we focus on the purity of the radio-selected subsamples (i.e. interpreting the matrix column-wise), rather than their completeness with respect to the reference classification. This distinction is particularly relevant for LSST-era applications, where the primary requirement is the

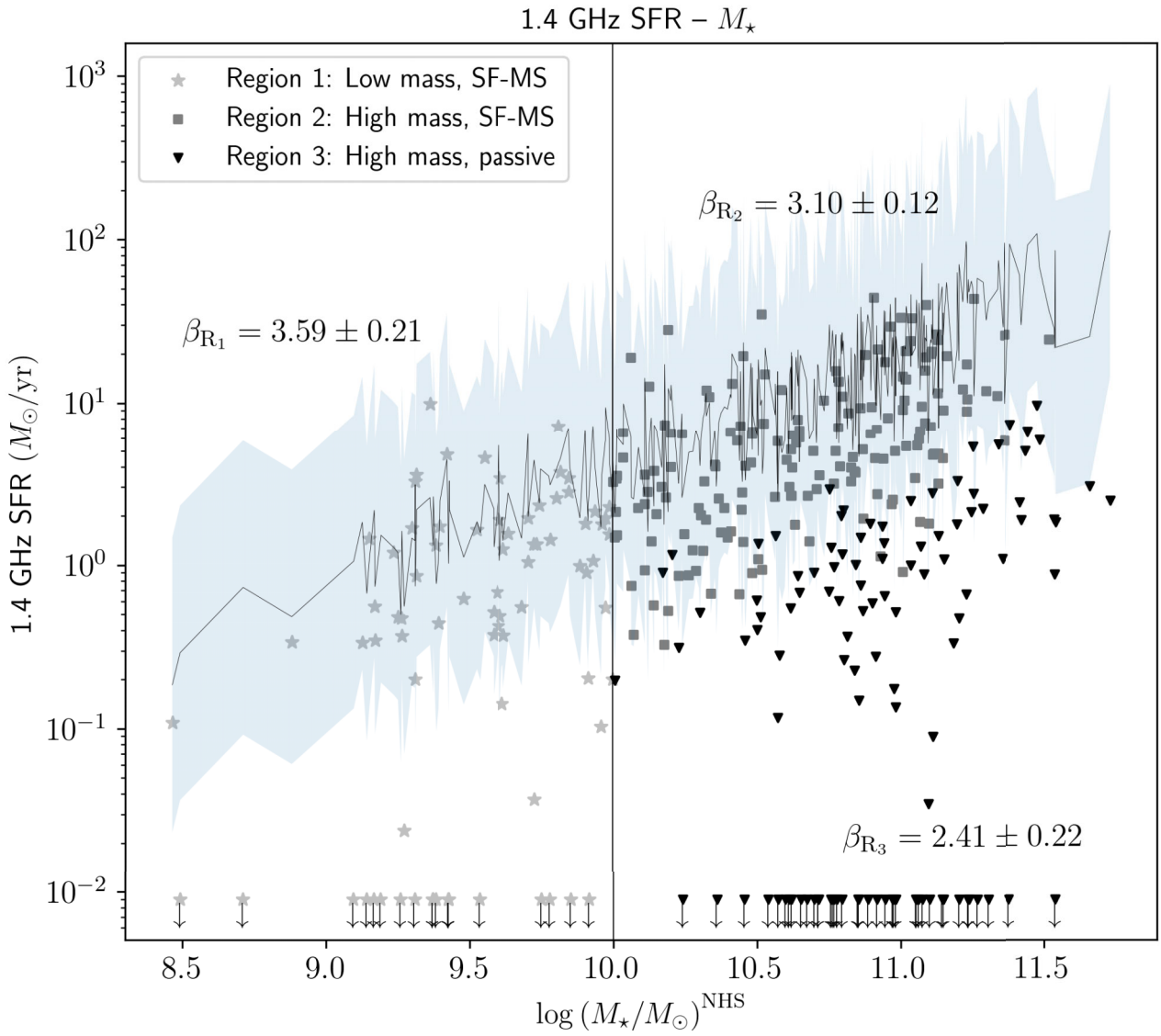

Figure 2. The distribution of SN Ia host galaxies across the 1.4 GHz SFR–M_* plane. The 1.4 GHz SFRs are computed directly in this work, whereas the galaxy stellar masses, M_* are determined and taken from Paper I. The plane is divided into three regions (coded by marker type) to isolate galaxies that are characterized by similar properties. Low-mass galaxies are indicated by stars, where we apply an arbitrary cut on mass at 10^{10}M$_\odot$. High-mass galaxies ($> 10^{10}$M$_\odot$) are then split into two populations based on whether they lie within a 3σ interval of the SF–MS, which is highlighted by the blue shaded region. High-mass, high SFR galaxies are shown by squares and conversely, high-mass, low SFR (passive) galaxies are shown as triangles. Galaxies with SFR values below 0.01 M$_\odot$yr^{-1} are set as upper limits to this value and are indicated by downward arrows for illustration purposes. Refer to Table 1 for a full summary of cosmological SN Ia nuisance parameter constraints.

construction of clean SN host galaxy populations rather than the recovery of all systems identified in higher-information analyses.

Under this interpretation, the radio-selected low-mass sample (Region 1) shows minimal contamination, with ∼96 per cent of galaxies in this category corresponding to the same region in the reference classification. This demonstrates that the low-mass region remains cleanly isolated on the SFR–$M_\star$ plane despite the removal of FIR measurements in the SED fitting.

For the high-mass populations (Regions 2 and 3), the agreement between the two classification schemes remains strong, though a higher degree of mixing is observed compared to the low-mass regime; expectedly, given that these regions are separated primarily by their star-formation properties and are therefore sensitive to the choice of SFR tracer. The radio-selected Region 2 sample exhibits a purity of ∼77 per cent, with the dominant contamination arising from galaxies assigned to the passive region in the reference classification (30 sources). Conversely, the radio-selected Region 3 sample exhibits a purity of ∼87 per cent, with most of the contamination arising from Region 2 in the reference sample (14 sources).

Some fraction of the off-diagonal population may arise from differences in tracer time-scales, particularly in systems with non-steady star formation histories (SFHs). R. H. W. Cook et al. (2024) find that galaxies with increasing SFHs can exhibit elevated SED-derived SFRs relative to their radio emission, which they attribute to the finite time required for supernova-driven

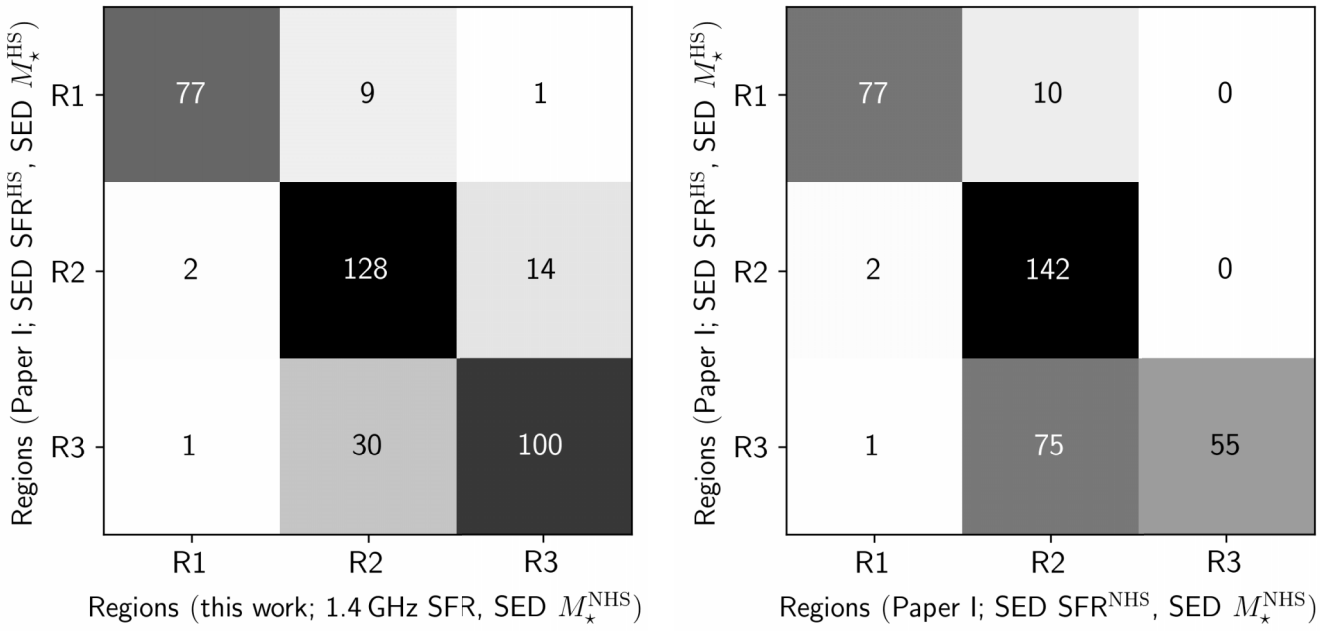

Figure 3. *Left*: Confusion matrix comparing region classifications from Paper I, based on SED-derived galaxy properties including *Herschel* and *Spitzer* ('HS') data, with region classifications from this work, based on 1.4 GHz-derived SFRs [computed using the R. H. W. Cook et al. (2024) relation] and SED-derived stellar masses excluding *Herschel* and *Spitzer* ('NHS') data. The values in each cell give the number of galaxies from a given Paper I region (rows) that are assigned to the corresponding region in this work (columns). *Right*: Same as left, but comparing Paper I region classifications based on SED-derived galaxy properties including ('HS') and excluding ('NHS') *Herschel* and *Spitzer* data.

radio emission to build up. Complementarily, R. C. Arango-Toro et al. (2023) show that galaxies with declining SFHs can exhibit radio-derived SFRs in excess of their instantaneous SED-derived SFRs, with roughly 30 per cent of their sample showing radio SFRs at least an order of magnitude higher, consistent with radio emission responding to changes in star formation over longer time-scales ($\sim$ 100 Myr). More generally, this behaviour may arise from the choice of adopted calibration or from systems lying near the star-forming-passive boundary. In addition to this overall scatter, the mixing appears asymmetric in nature, with a larger number of galaxies *misclassified* relative to the reference axis from the passive (Region 3) to the star-forming (Region 2) sample than vice versa. This may partly reflect low-level AGN activity, which can enhance radio emission without a corresponding increase in SED-based SFR estimates.

For completeness, Fig. 3 (right panel) shows a confusion matrix constructed in the same manner as the left panel, but with both SFRs and stellar masses derived from SED fitting excluding *Herschel* and *Spitzer* data (*x*-axis), while retaining the same reference (*y*-axis). The percentage of SN hosts assigned identically (i.e. along the diagonal) between the SED$^{\rm HS}$ and SED$^{\rm NHS}$ cases drops to 76 per cent.

When read column-wise, the Region 1 classifications in this matrix are unchanged relative to the left panel, as the SED-derived stellar masses in both matrices are derived without FIR data. The more informative comparison lies in the high-mass regime (Regions 2 and 3), where the separation is driven primarily by star-formation activity. For the SED$^{\rm NHS}$-selected Region 2 sample, substantial mixing is shown with the reference passive (Region 3) population, with a purity of 62 per cent. By contrast, the SED$^{\rm NHS}$-selected Region 3 sample consists of a much narrower subset of the passive population identified in Paper I, recovering fewer than half of the galaxies compared to the radio-based selection (left panel matrix), despite exhibiting minimal contamination. Such a reduced, contamination-free sample should not necessarily be interpreted as a cleaner representation of the same population, as it may instead preferentially select galaxies with particular SED characteristics in the absence of FIR constraints, thereby potentially introducing unquantifiable selection effects.

Quantifying the origin of this behaviour is not the focus of this work and we include the NHS case only for comparison, as many previous SN host studies rely on similarly limited wavelength coverage. We do not explore or comment on this further. Instead, our emphasis is on the radio-based classification, the use of which is more physically motivated (J. J. Condon 1992) and thus, forms the primary basis of our analysis. The strong diagonal dominance and high regional purities in the confusion matrix (Fig. 3, left panel) demonstrate that 1.4 GHz SFRs provide a robust and internally consistent alternative to FIR-based SED SFRs, preserving a broader and more representative high-mass population while maintaining a clear separation between regions on the SFR–$M_\star$ plane. However, as these inferences are drawn from the confusion matrix alone, we next assess their robustness by examining whether SN Ia subsamples based on the radio-selected regions exhibit consistent properties with those measured in Paper I.

3.2.2 *Nuisance parameter constraints*

In this section, we investigate the SN nuisance parameters (α, β) that are used to correct for variations in SN luminosities, as well as the absolute magnitude of SNe Ia (M in equation 1). We note, however, that without an absolute calibrated distance scale, M is degenerate with H_0. Instead, cosmological fits typically marginalize over a single parameter, $\mathcal{M} = M + \log_{10}(c/H_0) + 25$,

Table 1. Nuisance parameter values constrained for SNe Ia in host galaxies that occupy three distinct regions of the SFR–$M_\star$ plane for this work (based on 1.4 GHz SFRs) and the Paper I results (based on SED-derived SFRs), which are included solely for comparison.

	This work				Paper I			
SF–MS Region	N_{SN} [a]	α	β	$\Delta\mathcal{M}$ [b]	N_{SN}	α	β	$\Delta\mathcal{M}$
Full sample	358	0.162±0.011	3.14±0.09	–	495	0.157±0.009	3.11±0.08	–
Region 1: Low-mass, SF-MS	77	0.170±0.030	3.59±0.21	0.053±0.025	116	0.185±0.023	3.51±0.16	0.055±0.019
Region 2: High-mass, SF–MS	166	0.199±0.020	3.10±0.12	−0.010±0.017	197	0.180±0.019	3.15±0.11	0.000±0.015
Region 3: High-mass, passive	115	0.147±0.019	2.41±0.22	−0.042±0.020	182	0.172±0.013	2.12±0.16	−0.066±0.014

Notes.[a] The number of SNe Ia included in the BBC fit include a 4σ outlier rejection. For this reason, the BBC fit of the full sample for this work (362 SNe), for example, only includes 358 SNe.
[b] $\Delta\mathcal{M}$ is the difference in absolute brightness compared to the full 'gold' sample defined in this work, with the errors given in quadrature. The quoted uncertainties on $\Delta\mathcal{M}$ should be regarded as a conservative upper bound as the assumption of statistical independence – which underlies the quadrature addition of uncertainties – is not strictly valid in this case (each region sample is a sub-set of the gold sample which means the error on $\mathcal{M}$ for the gold sample and any region subsample are correlated). The true uncertainty on $\Delta\mathcal{M}$ is expected to be lower.

that combines these terms. Therefore, we do not present our results in terms of M, which requires an assumption for the value of H_0 but choose to report out findings in terms of $\Delta\mathcal{M}$, the relative value of $\mathcal{M}$ with respect to our full sample constraint. Full details of the procedures used in the computation of the parameters are presented in Paper I but, briefly, they are measured using the 'BEAMS with Bias Corrections' (BBC; R. Kessler & D. Scolnic 2017) framework. We obtain constraints both for our full sample and for the sub-samples of SNe Ia in each division of the 1.4 GHz SFR–M_* plane. Our results are presented in Table 1 and findings are as follows:

(i) The values of α in each of the three sub-regions are consistent, with the largest difference at the $\sim$1.9σ level (between Regions 2 and 3).
(ii) SNe Ia in low-mass hosts (Region 1) are characterized by higher values of β than those in high-mass hosts. The largest difference ($\sim$3.9σ) exists between Regions 1 and 3 (passive hosts). Smaller differences in β are seen between Regions 1 and 2 (high mass, MS), significant at the $\sim$2.0σ level. Differences persist between high-mass hosts (Regions 2 and 3), with passive hosts displaying the smallest β values ($\sim$2.8σ).
(iii) Consistent with previous works (P. L. Kelly et al. 2010; H. Lampeitl et al. 2010; M. Sullivan et al. 2010), we find SNe Ia in high-mass hosts (Regions 2 and 3) are, on average, brighter (negative $\Delta\mathcal{M}$) post-standardization than those in low-mass hosts. This well known trend is referred to as the 'mass step' and has been confirmed in previous cosmological analyses that fit the full SN Ia sample. The mass step is usually defined as the difference between the average Hubble residuals for low- and high-mass galaxies. As we are minimizing the residuals for each region separately, we instead look at differences in the SN absolute rest-frame magnitude across the three regions. The most significant brightness differences (0.095 mag) are seen between SNe Ia in low-mass (Region 1) and high-mass passive (Region 3) hosts, at a $\sim$3.0σ significance level. The smallest differences in brightness ($\sim$0.032 mag) are between SNe in both high mass regions ($\sim$1.2σ). Differences between low-mass and high-mass MS (Region 2) exist at the $\sim$2σ significance level.

While the qualitative trends observed here are similar to those reported in Paper I, the statistical significance of several inter-region differences changes when using radio-derived SFRs. This is expected, as the classification of host galaxies depends on the tracer used to characterize star formation activity, and the resulting redistribution of SNe between regions naturally alters the measured contrasts in the nuisance parameters.

Nevertheless, the nuisance parameters inferred in each region remain consistent with those obtained using SED-based SFR classifications at the $\sim$1.1σ level (see Table 1). Region 3 provides a particularly stringent test of the impact of SFR estimator choice on the inferred SN parameters. In Paper I, we demonstrate that the inferred value of β in Region 3 is particularly sensitive to contamination from SNe Ia associated with neighbouring star-forming galaxies, with the constraint responding systematically to shifts in the boundary between Regions 2 and 3 (see Paper I, fig. 9). The fact that the radio-SFR based analysis reproduces the Paper I results within the uncertainties indicates that radio SFRs offer a promising basis for partitioning galaxies in this parameter space, even in regimes where cross-region contamination effects are expected to be most pronounced.

We note that the Paper I values reported in Table 1 are derived from the primary 501-host 'gold' sample; repeating the SED-based Paper I analysis on the restricted 362-galaxy sub-set used here yields consistent nuisance parameter constraints.

Additionally, we verify that the stretch and colour distributions of SNe Ia in each of the three regions are consistent with those reported previously (see Paper I, fig. 10).

4 PREDICTIONS

A key question is whether current and forthcoming radio continuum surveys are sufficiently deep to distinguish star-forming from passive galaxies relative to the evolving SF–MS. This can be evaluated by converting the detection limit of a given radio survey into a corresponding star-formation rate threshold and comparing it with the evolving SF–MS as a function of redshift. Ambiguity arises when a radio non-detection may correspond to either a passive galaxy or an SFG below the survey sensitivity (complicating a robust separation between Regions 2 and 3). Formally, the condition for *complete* detection of SFGs can be generalized to,

$$\mathrm{SFR_{lim}}(z) \leq \mathrm{SFR_{MS}}(M_\star = 10^{10}\mathrm{M}_\odot, z) - 0.9\ \mathrm{dex}, \quad (6)$$

where $\mathrm{SFR_{lim}}(z)$ denotes the SFR corresponding to the survey radio detection threshold at redshift z, derived from the radio–SFR calibration of R. H. W. Cook et al. (2024, equation 4), and $\mathrm{SFR_{MS}}$ is the SFR of a galaxy of stellar mass $M_\star$ on the SF–MS at the same redshift, for which we take the SF–MS parametrization of K. E. Whitaker et al. (2012, equation 5). The offset of 0.9 dex

below the ridge line reflects our adopted definition of the lower boundary of the star-forming population, i.e. galaxies above this threshold are classified as SFGs (Region 2) and those below it as passive (Region 3). This condition is applied only to galaxies with $\geq 10^{10}\mathrm{M}_{\odot}$; systems below this threshold are assigned to Region 1 on the basis of stellar mass alone (constraints from optical/NIR surveys).

In what follows, we consider the redshift range over which the bulk of cosmologically useful SNe Ia are expected to be observed – focusing in practice on LSST – and examine how the depths of the overlapping radio surveys compare to the threshold defined by equation (6), and thus what they imply for the expected detectability and classification of SN Ia host galaxies.

We emphasize that equation (6) provides a simplified representation, as it relies on the choice of SF–MS parametrization and radio–SFR calibration as proxies for the underlying galaxy population, neither of which are *absolute*. Intrinsic scatter and various systematics are not explicitly accounted for, and the resulting limits on detectable SFR as a function of redshift should therefore be interpreted as approximate forecasts rather than exact thresholds.

4.1 Deep-field strategy: LSST Deep Drilling Fields (DDFs)–MIGHTEE

Radio coverage of the LSST Deep Drilling Fields (DDFs) is provided by the ongoing MIGHTEE survey (M. Jarvis et al. 2016), which will ultimately cover ∼20 deg^2. Over the DDFs, the bulk of cosmologically useful SNe Ia from LSST are expected to lie at $z \lesssim 1$ (A. Mitra et al. 2023). Taking $z = 1$ as the upper bound of the relevant range, we evaluate equation (6) using the current MIGHTEE survey rms sensitivity of ∼4μJy (1σ). The corresponding 3σ and 5σ detection thresholds translate into the dashed horizontal SFR limits shown in the top panel of Fig. 4, overlaid on the SF–MS and its adopted 0.9 dex envelope at this redshift. At $z = 1$, a galaxy with stellar mass $M_{\star} = 10^{10}\mathrm{M}_{\odot}$ lying on the SF–MS would be expected to have SFR $\sim 10\,\mathrm{M}_{\odot}\,\mathrm{yr}^{-1}$, comparable to the MIGHTEE 3σ depth. It would therefore be difficult to robustly place such a galaxy into Regions 2 or 3, under our adopted definition of the star-forming locus (shaded locus in Fig. 4).

However, since optical/NIR imaging from SN surveys will provide precise host galaxy positions a priori, forced photometry can be performed (as done in this work) which would allow for flux measurements below the nominal radio 3σ detection threshold. The depths at each redshift derived here should therefore be interpreted as conservative limits for direct (blind catalogue-level) detections, while deeper statistical constraints are achievable with positionally informed extraction techniques, for example, fully Bayesian source extraction based on the optical/NIR galaxy positions (e.g. E. D. Malefahlo et al. 2026).

For stellar masses $\sim 10^{11.5}\,\mathrm{M}_{\odot}$, the SFR increases by a factor of 10 to $M_{\star} = 10^{10}\,\mathrm{M}_{\odot}$, such that the full star-forming region lies above the 3σ radio limit; in this regime, a radio non-detection would reliably indicate a passive (Region 3) galaxy (though galaxies above this mass threshold comprise a relatively small fraction of the population).

4.2 Wide-field strategy: LSST Wide-Fast-Deep (WFD)–ASKAP EMU

For the LSST Wide-Fast-Deep (WFD) survey, the majority of SNe Ia relevant for cosmological analyses are expected at $z \lesssim 0.5$ (see

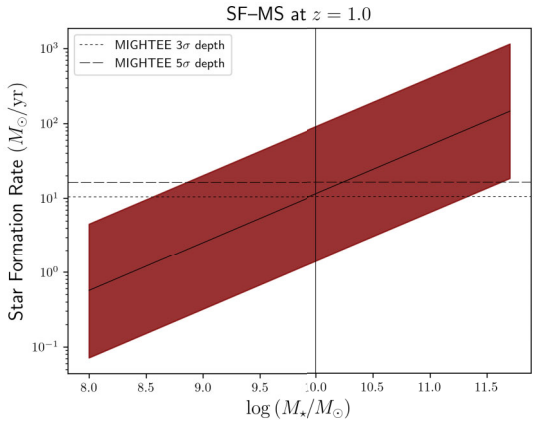

(a) LSST DDFs with MeerKAT/MIGHTEE (rms = 4μJy) at z = 1.

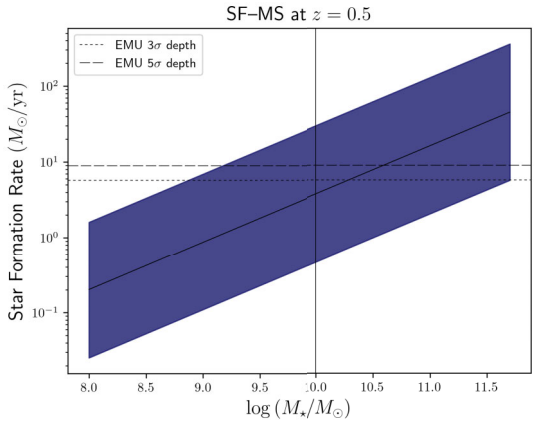

(b) LSST WFD with ASKAP/EMU (rms = 10μJy) at z = 0.5.

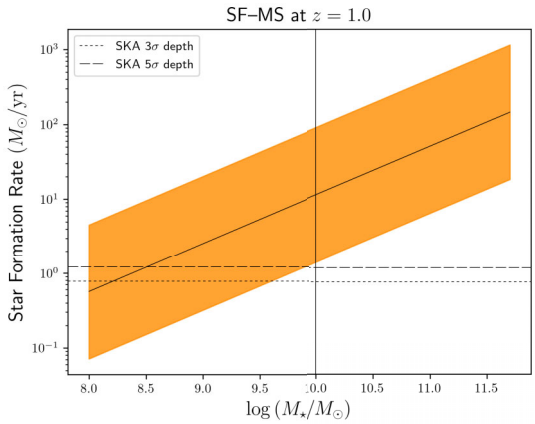

(c) Prospective SKAO deep fields (rms = 0.2μJy) overlapping LSST DDFs and future Roman SN fields at z = 1.

Figure 4. SF–MS compared to radio detection thresholds at redshifts relevant for SN cosmology. The solid line shows the adopted SF–MS parametrization at the indicated redshift, while the shaded region denotes the star-forming population (Region 2) defined as ±0.9 dex about the ridge line (with the lower boundary marking the transition to passive systems; Region 3). Horizontal dashed lines indicate the 3σ and 5σ radio detection limits converted to SFRs using the adopted radio–SFR calibration (equation 4). The vertical line marks $M_{\star} = 10^{10}\mathrm{M}_{\odot}$, above which the completeness criterion of equation (6) is evaluated. The comparison illustrates the redshift-dependent ability of current and future radio surveys to unambiguously distinguish star-forming from passive SN Ia host galaxies.

SN Ia redshift distribution expected from the Time Domain Extragalactic Survey conducted on the 4-metre Multi-Object Spectroscopic Telescope; C. Frohmaier et al. 2025, figs 10 and 11). This limit is mainly set by the requirement that a spectroscopic redshift be obtained for the SN host galaxy, as is standard practice in SN cosmological analyses. Across this footprint, radio observations are available from the Australian SKA Pathfinder-Evolutionary Map of the Universe (ASKAP-EMU; R. P. Norris et al. 2011; A. Hopkins et al. 2025) survey, reaching an rms sensitivity of $\sim 10\mu$Jy. At $z = 0.5$, the corresponding 3σ and 5σ SFR limits are shown as dashed horizontal lines in the middle panel of Fig. 4.

4.3 Future prospects

Further into the future the Square Kilometre Array Observatory (SKAO) has the potential to reach depths comparable to those of MIGHTEE, but over thousands of square degrees (I. Prandoni & N. Seymour 2015). This combination of depth and area will enable radio-based SFR measurements for SN host galaxies across the wide-area footprints of future transient surveys, including those conducted with Roman, whose SN Ia sample is expected to have a median redshift of $z \sim 1$ and extend to $z \sim 2.5$ (B. M. Rose et al. 2025, fig. 6).

In addition to wide-area coverage, dedicated SKAO continuum deep fields are anticipated, likely overlapping the Rubin/LSST DDFs and reaching an rms sensitivity of $S_{1.4} \sim 0.2\mu$Jy, roughly a factor of 20 deeper than our current deepest data on these fields (see e.g. M. Jarvis et al. 2015; I. Prandoni & N. Seymour 2015). At $z = 1$, the anticipated SKAO deep-field sensitivity places both the 3σ and 5σ detection limits below the SF–MS envelope for galaxies with $M_\star > 10^{10}\,\mathrm{M}_\odot$ (bottom panel of Fig. 4), such that a radio non-detection would unambiguously correspond to a passive (Region 3) system. This continues to hold up to $z > 2$, although, given the evolution in the SF–MS, there are a relative scarcity of passive galaxies at these redshifts.

It is worth noting that this depth (0.2 μJy) far exceeds the equivalent depth for SFR of existing FIR data over these fields from *Herschel* (S. J. Oliver et al. 2012), Submillimetre Common-User Bolometer Array2 (SCUBA2; J. E. Geach et al. 2017), and the *Wide-field Infrared Explorer* (WISE; E. L. Wright et al. 2010), making the radio continuum one of the most efficient probes of the total star-formation of a galaxy (see e.g. D. J. B. Smith et al. 2021; R. K. Cochrane et al. 2023; N. J. Thykkathu et al. 2026; R. G. Varadaraj et al. 2026).

The principle advantage of SKAO over MeerKAT (whose MIGHTEE survey currently covers the DDFs), however, is not only its nominal sensitivity, but the fact that the SKAO will have sufficient angular resolution to not be predominantly impacted by the confusion limit. In contrast, the effective depth of MIGHTEE is limited by confusion noise at its ~ 5 arcsec resolution, rather than by thermal noise, typically reducing the achievable sensitivity by a factor of $\sim 2-3$. The future use of radio continuum surveys for separating SN host galaxies into star-forming and passive systems (Regions 2 and 3) will therefore be impactful over the next decade. This will be critical for fully exploiting the optical and near-infrared datasets from LSST and *Euclid* for SN cosmology.

5 CONCLUSIONS

In this paper, we model the distribution of DES SN Ia host galaxies on the SFR–$M_\star$ plane using SFRs calibrated from 1.4 GHz luminosities, and compare these results with our previous work based on SED-derived SFR measurements incorporating UV-to-FIR photometry. We identify three regions within the 1.4 GHz SFR–$M_\star$ plane, corresponding to low-mass hosts, high-mass star-forming hosts and high-mass passive hosts. Our main findings are as follows:

(i) Across all three regions, 84 per cent of SN Ia host galaxies retain the same regional classification as in our analysis based on using full UV-to-FIR SED-derived SFRs.

(ii) The low-mass region shows the highest level of consistency between both analyses, with a 96 per cent classification agreement. This is expected, as stellar masses are primarily constrained by optical/NIR photometry in the SED-fitting, and these data remain unchanged between this work and our previous paper.

(iii) Differences are primarily confined to the high-mass regime, reflecting the sensitivity of the star-forming–passive division on the adopted star-formation estimator. Nevertheless, the high-mass star-forming and passive populations show strong overall consistency between the radio- and SED-derived classifications, with 77 per cent and 87 per cent classification agreement, respectively.

(iv) We also measure SN Ia nuisance parameters (α, β, M) for SNe in each host galaxy region of the 1.4 GHz SFR–$M_\star$ plane. The slope of the SN colour-luminosity relation (β) continues to show a dependence on the region of the SFR–$M_\star$ plane occupied by the SN host galaxies; SNe Ia in high-mass, passive systems yield the lowest value of $\beta = 2.41 \pm 0.22$ (a $\sim 3.9\sigma$ difference relative to low-mass hosts). SNe Ia in high-mass hosts are also brighter post-standardisation than those in low-mass hosts, with the largest magnitude difference of 0.095 mag observed between low-mass and high-mass passive hosts at the 3σ level. The statistical significances of some inter-region comparisons differ between the radio-based and SED-based host classifications, as expected given the redistribution of SNe between regions when adopting a different SFR tracer. Nevertheless, the inferred nuisance parameters from the two analyses agree within $\lesssim 1.1\sigma$ across all regions, consistent with statistical fluctuations. The persistence of region-dependent trends within the radio-defined host populations therefore provides independent confirmation for the environmental dependence of SN Ia properties identified in our previous study.

Historically, the limiting systematic for SN Ia analyses has been photometric calibration. We are now entering a transitional phase in SN cosmology in which host-galaxy-dependent effects are emerging as the dominant contribution to the systematic uncertainty budget (M. Vincenzi et al. 2024). To model environmental dependencies, cosmological analyses typically implement a host galaxy stellar-mass-dependent correction. Stellar mass is favoured as the environmental proxy because it exhibits a measurable correlation with SN luminosities and for the practical advantage that it can be robustly estimated even when host photometric data are limited. Despite its utility and widespread adoption, there is mounting evidence that this single-parameter treatment provides an incomplete description of the host-environment dependence of SN Ia luminosities. In particular, empirical trends between SN Ia standardization parameters and galaxy SFR suggest that additional environmental information is encoded beyond that captured by mass alone. This points towards the possibility that future iterations of the standardization framework may require inclusion of SFR alongside galaxy mass.

The implementation of this approach is fundamentally challenged by the need for accurate and internally consistent SFR measurements. Full UV-to-FIR SED fitting is widely regarded

as one of the most reliable diagnostics of SFR. The required longer-wavelength coverage will not, however, be uniformly available across the entire footprints of forthcoming surveys such as LSST and *Roman*. This will preclude a fully self-consistent derivation of galaxy SFRs from SED-fitting alone, rendering the measurements dependent on spatial variations in wavelength coverage. Instead, robust characterization of the star-formation activity of SN Ia hosts will require a combined multitracer approach.

The radio continuum provides one such option, offering a powerful and dust-unbiased tracer of star-formation activity. Of course, as with any tracer, there are several factors in its application that still require careful consideration. One being the choice of literature radio–SFR calibration (see Appendix A). Given that these region definitions are used to construct SN Ia sub-samples, any calibration-dependent mixing among them propagates directly into the inferred nuisance parameters. This dependence can, however, be incorporated into the cosmological analysis by treating the calibration choice as a methodological systematic. For example, in the absence of a uniquely preferred calibration, the cosmological fit can be evaluated under a set of plausible calibrations, and the resulting variation in recovered parameters folded into the overall uncertainty budget. Another consideration is the characteristic time-scale probed by radio emission (of order $\sim$100 Myr), which differs from that of more instantaneous SFR (e.g. SED-based) tracers, and whose implications remain to be fully understood. Nevertheless, with charting the cosmic star-formation history as a central objective, the SKA will establish an era in which radio-derived SFRs – refined through sustained calibration efforts – become the de facto standard in modern galaxy evolution studies (E. J. Murphy 2009; M. Jarvis et al. 2015). This work establishes a roadmap for integrating 1.4 GHz derived SFRs into SN Ia host studies, enabling environmental characterization commensurate with future SN experiments, and thereby unlocking their full cosmological potential.

Beyond the practical demands inherent to host galaxy classification at scale, the LSST era will likely also necessitate a reassessment of the current implementation of SN Ia cosmology. One such shift will be the construction of environmentally defined sub-samples, for example, by restricting analyses to SNe Ia in SF, low-mass hosts (as suggested by M. J. Childress, C. Wolf & H. J. Zahid 2014; L. Kelsey et al. 2023) or to passive galaxies (as suggested by R. Chen et al. 2022). This shift will foreground new, previously secondary considerations, including uncertainties in host-galaxy classification arising from differences between choice of SFR estimator and/or calibration, contamination between environmental categories (e.g. passive hosts misidentified as star forming), and the accurate modelling of novel selection effects. Considerations that, taken together, will reshape the structure of the systematic error budget, as even modest levels of environment misclassification propagate into non-negligible biases in SN Ia standardization and cosmological inference. Against this backdrop, a central question remains unanswered: do our cosmological results vary significantly when derived from sub-samples of SNe Ia occupying distinct host environments?

ACKNOWLEDGEMENTS

The authors gratefully acknowledge Catherine Hale for their assistance. The authors additionally wish to thank the anonymous reviewer for their detailed comments, which helped to substantially improve the manuscript. SR, MJJ, MV, and IHW acknowledge support from the Oxford Hintze Centre for Astrophysical Surveys which is funded through generous support from the Hintze Family Charitable Foundation. MJJ also acknowledges the support of a UKRI Frontiers Research Grant (EP/X026639/1), which was selected by the European Research Council. MV was supported by UKRI Future Leaders Fellowship (UKRI2363). MS acknowledges support from the Science and Technology Facilities Council (STFC) grant ST/Y001850/1.

DATA AVAILABILITY

The DES-SN5YR data are all in the public domain (B. O. Sánchez et al. 2024)[2]. The MIGHTEE continuum DR1 data used in this work are released with C. L. Hale et al. (2025).

REFERENCES

Arango-Toro R. C., Ciesla L., Ilbert O., Magnelli B., Jiménez-Andrade E. F., Buat V., 2023, A&A, 675, A126
Astier P. et al., 2006, A&A, 447, 31
Bell E. F., 2003, ApJ, 586, 794
Böckmann K. et al., 2023, A&A, 678, A56
Boselli A., Fossati M., Gavazzi G., Ciesla L., Buat V., Boissier S., Hughes T. M., 2015, A&A, 579, A102
Bruzual G., Charlot S., 2003, MNRAS, 344, 1000
Bundy K., Fukugita M., Ellis R. S., Targett T. A., Belli S., Kodama T., 2009, ApJ, 697, 1369
Calzetti D. et al., 2007, ApJ, 666, 870
Calzetti D. et al., 2010, ApJ, 714, 1256
Carnall A. C., McLure R. J., Dunlop J. S., Davé R., 2018, MNRAS, 480, 4379
Chabrier G., 2003, PASP, 115, 763
Charlot S., Fall S. M., 2000, ApJ, 539, 718
Chen R. et al., 2022, ApJ, 938, 62
Childress M. et al., 2013, ApJ, 770, 108
Childress M. J., Wolf C., Zahid H. J., 2014, MNRAS, 445, 1898
Cochrane R. K. et al., 2023, MNRAS, 523, 6082
Condon J. J., 1992, ARA&A, 30, 575
Conroy C., 2013, ARA&A, 51, 393
Conselice C. J., Yang C., Bluck A. F. L., 2009, MNRAS, 394, 1956
Cook R. H. W. et al., 2024, MNRAS, 531, 708
Cortese L., Boselli A., Franzetti P., Decarli R., Gavazzi G., Boissier S., Buat V., 2008, MNRAS, 386, 1157
D'Andrea C. B. et al., 2011, ApJ, 743, 172
da Cunha E., Charlot S., Elbaz D., 2008, MNRAS, 388, 1595
Daddi E. et al., 2007, ApJ, 670, 156
Dalla Vecchia C., Schaye J., 2008, MNRAS, 387, 1431
Darvish B., Mobasher B., Sobral D., Rettura A., Scoville N., Faisst A., Capak P., 2016, ApJ, 825, 113
Davies L. J. M. et al., 2016, MNRAS, 461, 458
Davies L. J. M. et al., 2017, MNRAS, 466, 2312
Davies L. J. M. et al., 2019, MNRAS, 483, 5444
de Jong T., Klein U., Wielebinski R., Wunderlich E., 1985, A&A, 147, L6
Elbaz D. et al., 2007, A&A, 468, 33
Fabian A. C., 2012, ARA&A, 50, 455
Flaugher B. et al., 2015, AJ, 150, 150
Frohmaier C. et al., 2025, ApJ, 992, 158
Geach J. E. et al., 2017, MNRAS, 465, 1789
Gordon K. D., Clayton G. C., Witt A. N., Misselt K. A., 2000, ApJ, 533, 236
Gunawardhana M. L. P. et al., 2011, MNRAS, 415, 1647
Guy J. et al., 2007, A&A, 466, 11
Haarsma D. B., Partridge R. B., Windhorst R. A., Richards E. A., 2000, ApJ, 544, 641
Hale C. L. et al., 2023, MNRAS, 520, 2668
Hale C. L. et al., 2025, MNRAS, 536, 2187

Hao C.-N., Kennicutt R. C., Johnson B. D., Calzetti D., Dale D. A., Moustakas J., 2011, ApJ, 741, 124
Helou G., Soifer B. T., Rowan-Robinson M., 1985, ApJ, 298, L7
Heywood I. et al., 2022, MNRAS, 509, 2150
Heywood I. et al., 2024, MNRAS, 534, 76
Hirashita H., Buat V., Inoue A. K., 2003, A&A, 410, 83
Hopkins A. et al., 2025, PASA, 42, e071
Hopkins A. M. et al., 2003, ApJ, 599, 971
Hounsell R. et al., 2018, ApJ, 867, 23
Iglesias-Páramo J. et al., 2006, ApJS, 164, 38
Ivezić Ž. et al., 2019, ApJ, 873, 111
Jarvis M. et al., 2015, The star-formation history of the Universe with the SKA, Advancing Astrophysics with the Square Kilometre Array (AASKA14). p. 68
Jarvis M. et al., 2016, The MeerKAT International GHz Tiered Extragalactic Exploration (MIGHTEE) Survey, MeerKAT Science: On the Pathway to the SKA, p. 6
Jarvis M. J. et al., 2010, MNRAS, 409, 92
Johnston R., Vaccari M., Jarvis M., Smith M., Giovannoli E., Häußler B., Prescott M., 2015, MNRAS, 453, 2540
Kauffmann G., White S. D. M., Heckman T. M., Ménard B., Brinchmann J., Charlot S., Tremonti C., Brinkmann J., 2004, MNRAS, 353, 713
Kauffmann G., Heckman T. M., De Lucia G., Brinchmann J., Charlot S., Tremonti C., White S. D. M., Brinkmann J., 2006, MNRAS, 367, 1394
Kelly P. L., Hicken M., Burke D. L., Mandel K. S., Kirshner R. P., 2010, ApJ, 715, 743
Kelsey L. et al., 2023, MNRAS, 519, 3046
Kennicutt Jr R. C., 1998, ARA&A, 36, 189
Kennicutt R. C., Evans N. J., 2012, ARA&A, 50, 531
Kennicutt Jr R. C. et al., 2009, ApJ, 703, 1672
Kenworthy W. D. et al., 2021, ApJ, 923, 265
Kessler R., Scolnic D., 2017, ApJ, 836, 56
Kroupa P., 2001, MNRAS, 322, 231
Lampeitl H. et al., 2010, ApJ, 722, 566
Lotz J. M., Jonsson P., Cox T. J., Croton D., Primack J. R., Somerville R. S., Stewart K., 2011, ApJ, 742, 103
Madau P., Dickinson M., 2014, ARA&A, 52, 415
Maddox N. et al., 2021, A&A, 646, A35
Malefahlo E. D. et al., 2026, MNRAS, 547, stag285
Mauch T., Sadler E. M., 2007, MNRAS, 375, 931
McAlpine K., Smith D. J. B., Jarvis M. J., Bonfield D. G., Fleuren S., 2012, MNRAS, 423, 132
Miller G. E., Scalo J. M., 1979, ApJS, 41, 513
Mitra A., Kessler R., More S., Hlozek R., LSST Dark Energy Science Collaboration, 2023, ApJ, 944, 212
Murphy E. J., 2009, ApJ, 706, 482
Murphy E. J. et al., 2011, ApJ, 737, 67
Noeske K. G. et al., 2007, ApJ, 660, L43
Noll S., Burgarella D., Giovannoli E., Buat V., Marcillac D., Muñoz-Mateos J. C., 2009, A&A, 507, 1793
Norris R. P. et al., 2011, PASA, 28, 215
Oliver S. J. et al., 2012, MNRAS, 424, 1614
Pacifici C. et al., 2023, ApJ, 944, 141
Papovich C., Dickinson M., Ferguson H. C., 2001, ApJ, 559, 620
Paul S. et al., 2025, preprint (arXiv:2512.11964)
Peng Y.-j. et al., 2010, ApJ, 721, 193
Planck Collaboration VI, 2020, A&A, 641, A6
Ponomareva A. A. et al., 2021, MNRAS, 508, 1195
Ponomareva A. A. et al., 2023, MNRAS, 522, 5308
Prandoni I., Seymour N., 2015, Revealing the Physics and Evolution of Galaxies and Galaxy Clusters with SKA Continuum Surveys, Advancing Astrophysics with the Square Kilometre Array (AASKA14), p. 67
Ramaiya S., Vincenzi M., Jarvis M. J., Wiseman P., Sullivan M., 2025, MNRAS, 543, 2180 (Paper I)
Robotham A. S. G., Bellstedt S., Lagos C. d. P., Thorne J. E., Davies L. J., Driver S. P., Bravo M., 2020, MNRAS, 495, 905
Rose B. M. et al., 2021, preprint (arXiv:2111.03081)
Rose B. M. et al., 2025, ApJ, 988, 65
Salpeter E. E., 1955, ApJ, 121, 161
Sánchez B. O. et al., 2024, ApJ, 975, 5
Sancisi R., Fraternali F., Oosterloo T., van der Hulst T., 2008, A&AR, 15, 189
Scannapieco C., Tissera P. B., White S. D. M., Springel V., 2008, MNRAS, 389, 1137
Schawinski K. et al., 2014, MNRAS, 440, 889
Schreiber C. et al., 2015, A&A, 575, A74
Smith D. J. B. et al., 2021, A&A, 648, A6
Smith M. et al., 2020, MNRAS, 494, 4426
Speagle J. S., Steinhardt C. L., Capak P. L., Silverman J. D., 2014, ApJS, 214, 15
Sullivan M., Mobasher B., Chan B., Cram L., Ellis R., Treyer M., Hopkins A., 2001, ApJ, 558, 72
Sullivan M. et al., 2006, ApJ, 648, 868
Sullivan M. et al., 2010, MNRAS, 406, 782
Tabatabaei F. et al., 2025, ApJ, 989, 44
Taylor A. R. et al., 2024, MNRAS, 528, 2511
The Dark Energy Survey Collaboration, 2005, preprint (astro–ph/0510346)
Thykkathu N. J. et al., 2026, MNRAS, preprint (arXiv:2601.14913)
Tripp R., 1998, A&A, 331, 815
Varadaraj R. G. et al., 2026, MNRAS, 547, stag473
Vincenzi M. et al., 2024, ApJ, 975, 86
Whitaker K. E., van Dokkum P. G., Brammer G., Franx M., 2012, ApJ, 754, L29
Whitaker K. E. et al., 2014, ApJ, 795, 104
Whittam I. H. et al., 2022, MNRAS, 516, 245
Whittam I. H. et al., 2025, MNRAS, 543, 507
Wilman R. J. et al., 2008, MNRAS, 388, 1335
Wright E. L. et al., 2010, AJ, 140, 1868
Yun M. S., Reddy N. A., Condon J. J., 2001, ApJ, 554, 803

APPENDIX A: CONFUSION MATRICES WITH ALTERNATIVE RADIO–SFR CALIBRATIONS

As a robustness check, we explore the impact of radio–SFR calibration choice on galaxy-region classifications by comparing confusion matrices for the J. J. Condon (1992), E. F. Bell (2003), and L. J. M. Davies et al. (2017) prescriptions, shown in Fig. A1. The overall structure of the confusion matrices is preserved, although there is a systematic increase in off-diagonal scatter relative to the fiducial case (R. H. W. Cook et al. 2024), most notably for the J. J. Condon (1992) relation. These differences are consistent with the distinct assumptions underlying each relation. In particular, the calibrations are normalized using different definitions of SFR and treatments of the radio emission components, while the L. J. M. Davies et al. (2017) relation is empirically tied to SED-based SFRs (as used in this work) but derived from a relatively small sample. As such, variations at this level are expected when applying these prescriptions to different datasets. We note that the R. H. W. Cook et al. (2024) calibration adopted in the main analysis (Fig. 3) was chosen prior to performing these comparisons and not in an attempt to maximize agreement between classification schemes.

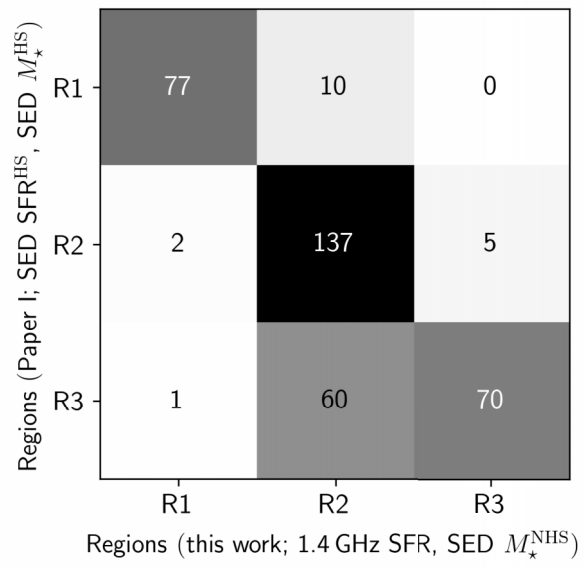

(a) Condon (1992) calibration.

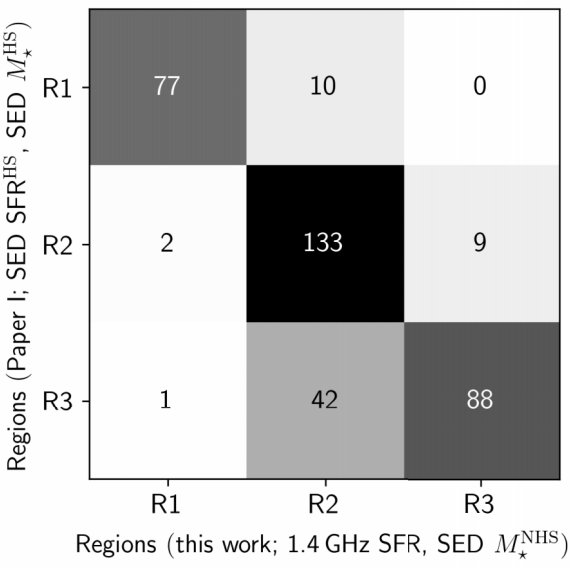

(b) Bell (2003) calibration.

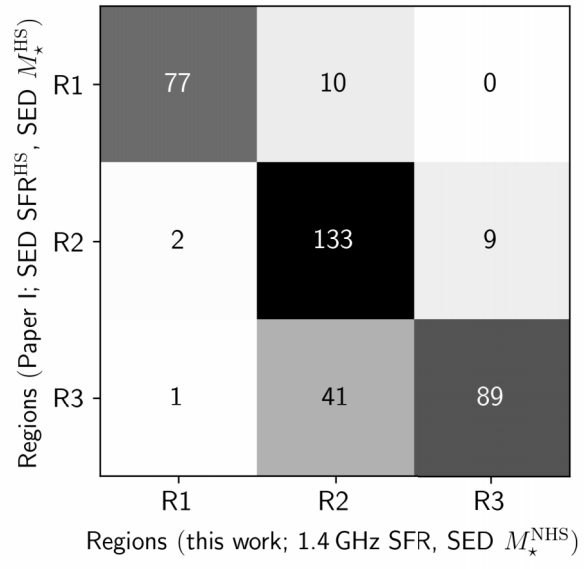

(c) Davies et al. (2017) calibration.

Figure A1. Confusion matrices comparing the galaxy-region classifications from Paper I (rows), based on SED-derived properties including *Herschel* and *Spitzer* data, with those obtained in this work (columns) using 1.4 GHz SFRs. As in Fig. 3, but with radio-derived SFRs computed using the J. J. Condon (1992), E. F. Bell (2003), and L. J. M. Davies et al. (2017) calibrations in place of the R. H. W. Cook et al. (2024) relation used in our fiducial analysis. Cell values give the number of galaxies in each pairing.

This paper has been typeset from a TEX/LATEX file prepared by the author.